Heavy ion acceleration in the Radiation Pressure Acceleration and Relativistic Induced Transparency regimes

G. M. Petrov[1], C. McGuffey[2], A. G. R. Thomas[3,4], K. Krushelnick[4] and F. N. Beg[2]

[1]Naval Research Laboratory, Plasma Physics Division, 4555 Overlook Ave. SW, Washington, DC 20375, USA

[2]Mechanical and Aerospace Engineering and Center for Energy Research, University of California-San Diego, La Jolla, CA 92093 USA

[3]Department of Physics, Lancaster University, Lancaster LA1 4YB UK

[4]Center for Ultrafast Optical Science, University of Michigan, Ann Arbor, MI 48109 USA

e-mail: george.petrov@nrl.navy.mil

PACS: 52.38.-r, 52.38.Ph, 52.50.Jm

04/17/2017

Abstract

We present a theoretical study of heavy ion acceleration from ultrathin (20 nm) gold foil irradiated by high-intensity sub-picosecond lasers. Using two-dimensional particle-in-cell simulations, three laser systems are modelled that cover the range between femtosecond and picosecond pulses. By varying the laser pulse duration we observe a transition from Radiation Pressure Acceleration to the Relativistic Induced Transparency regime for heavy ions akin to light ions. The underlying physics of beam formation and acceleration is similar for light and heavy ions, however, nuances of the acceleration process make the heavy ions more challenging. A more detailed study involving variation of peak laser intensity I_0 and pulse duration τ_{FWHM} revealed that the transition point from Radiation Pressure Acceleration to Relativistic Induced Transparency regime depends on the peak laser intensity on target and occurs for pulse duration $\tau_{FWHM}^{RPA \to RIT}[fs] \cong 210 / \sqrt{I_0[W/cm^2]/10^{21}}$. The most abundant gold ion and charge-to-mass ratio are Au^{51+} and $q/M \approx 1/4$, respectively, half that of light ions. For ultrathin foils, on the order of one skin depth, we established a linear scaling of the maximum energy per nucleon $(E/M)_{max}$ with $(q/M)_{max}$, which is more favorable than the quadratic one found previously. The numerical simulations predict heavy ions beams with very attractive properties for applications: high directionality (<10 degrees half-angle), high fluxes ($>10^{11}$ ions/sr) and energy (>20 MeV/nucleon) from laser systems delivering >20 J of energy on target.

1. Introduction

Ion beams generated from high-Z material are useful for many applications [1,2,3] such as nuclear reactions [4,5], production of super-heavy elements [6], exotic isomers and isotopes for biomedical use, fast ignition fusion, radiation effects in materials [7], medical applications including radiotherapy [8] and radiation oncology [9] and studies of exotic phenomena such as systems relevant to the interior of stars. So far, research has been conducted using conventional accelerators at enormously large and expensive facilities, however, short pulse lasers with duration <1 ps are emerging as a viable alternative tool for their production, making possible laboratory experiments at much lower cost. Laser-driven accelerators can generate heavy ion beams with energy in excess of 1 GeV, high directionality (<10 degree) and large fluxes (>10^{11} ion/sr). But in spite of their potential, short pulse lasers are still unexplored as drivers of heavy ions beams, although possible applications have already been discussed in a recent paper by Nishiuchi *et al.* [10]. The development of the next generation compact accelerators suitable to drive heavy ion beams depends critically on the understanding of the acceleration process and nuances pertinent to heavy ions, selecting a suitable set of laser parameters (intensity, pulse duration and spot size) and quantifying the parameters of the ion beam (energy and charge distribution, flux and directionality).

In our previous publication, we studied theoretically the generation of heavy ion beams driven by a short pulse laser with duration 32 fs and intensity >10^{21} W/cm^2 using 2D particle-in-cell (PIC) simulations [11]. The gold ions were accelerated due to either Target Normal Sheath Acceleration (TNSA) [12] or Radiation Pressure Acceleration (RPA) [13,14,15,16,17], depending on the foil thickness. For very thin foils, <100 nm, the RPA regime dominates the acceleration of the highest energy particles over TNSA. In this regime ion beams with energy of up to ~10 MeV/nucleon can be generated with conversion efficiency of 8 % at 27 Joules of laser energy on target. But the advantage of RPA was blemished by the realization that a number of challenges must be overcome in order to successfully accelerate heavy ions. They are rooted in the limited charge-to-mass ratio q/M, which results in lower energy per nucleon E/M compared to light ions due to the quadratic scaling $E/M \sim (q/M)^2$ [18,19]. In particular, numerical simulations including ionization physics established that for gold ions $q/M < 0.3$. Due to the low q/M, it takes longer to accelerate the ions. On top of that only half of the laser pulse can be utilized for acceleration, since the ions must be first ionized to high charge states, which occurs near the peak of the pulse, before being accelerated. The only experiment to date with short pulses (~40 fs) and thin Au foils (14 nm) [20] yielded maximum gold ion energies of less than 1 MeV/nucleon. These issues (low q/M and

shortened acceleration time) can, in principle, be overcome by increasing the laser intensity, however, that may invoke other problems such as interaction with pre-pulses and pre-expansion of the foil.

An alternative approach is to use longer, picosecond pulses, which provide ample acceleration time and eliminate the hurdles discussed above. It is widely recognized and proved experimentally that picosecond pulses work well for protons and light ions in the so-called Breakout Afterburner (BoA) regime [21,22,23,24,25] or Relativistic Induced Transparency (RIT) regime [26,27,28]. The focus in these experiments was on light ions, although there were experiments with mid-Z materials (Pd) [29,30]. To date, neither BoA nor RIT have been tested for high-Z materials. To our knowledge, there is only one experimental work with long (~1 ps) pulses involving heavy ion acceleration, but unusually thick (2 mm) lead foils were used [31]. The lack of experimental data, as well as the absence of theoretical works and understanding of the acceleration mechanisms pertinent to heavy ions is the primary motivation of this work. Specifically, the main goal is to extend the study of heavy ion acceleration from femtosecond to picosecond pulses, explore different regimes of ion acceleration (RPA and RIT) and show the transition between them. For this purpose we consider modeling existing laser systems with different pulse durations: femtosecond (the Bella laser at the Lawrence Berkeley National Laboratory), picosecond (the Trident laser at Los Alamos National Laboratory) and an intermediate one with pulse duration 180 fs (the Texas Petawatt Laser at the University of Austin, TX). In Section 2 we discuss the RPA-to-RIT transition for these laser systems by carrying out 2D3P PIC numerical simulations for Au ion acceleration from sub-micron foils and in Section 3 we discuss the beam parameters of gold ions and protons. Having pulse durations which differ by a factor of twenty raises an intriguing question: are long pulses at moderate intensities better than short pulses at high intensity? Section 4 discusses the RPA-to-RIT transition point by varying both the laser pulse duration and intensity. At the end of the section we propose a simple formula separating RPA from RIT as a function of peak laser intensity. In Section 5 we address the impact of charge-to-mass ratio on ion acceleration since this is one of the most critical issues related to heavy ion acceleration. Unlike previous studies, we observe scaling of the maximum energy per nucleon that is not as restrictive and sets the foundation for efficient acceleration of heavy ions. A discussion and summary are given in Section 6.

2. Transition from RPA to RIT for the Bella, Texas Petawatt and Trident lasers

Numerical simulations are performed using the two-dimensional electromagnetic PIC code outlined in Refs. [32,33]. In all cases the target is a flat 20 nm Au foil covered with a 5 nm

contaminant layer residing on the back of the foil, located at spatial position $x_0 = 48 \, \mu m$. For numerical purposes, the contaminants are modeled as a thin sheet of water at liquid density. The laser, target and simulation parameters are listed in Table 1. For each laser system the laser beam parameters were taken as close to the actual ones as possible for the following reason. Even though the primary goal is a basic study of heavy ion acceleration driven by short and long pulses, it is equally important to simulate real laser systems and to identify the ion acceleration mechanism pertinent to each one of them. The vastly different pulse duration of the three laser systems prompted us to compromise: the laser intensity was decreased when the pulse duration increased, since it was recognized that laser energy is the leading parameter [11]. We can still identify the ion acceleration mechanisms without keeping the laser intensity constant.

A sketch of the computational domain and target is shown in Figure 1. The computational domain dimensions L_x (length) and L_y (width) must be big enough to keep the particles inside the computational box throughout the simulations. For the Bella and Texas Petawatt lasers we chose $100 \times 128 \ \mu m^2$, but for the Trident laser it was necessary to increase it to $200 \times 256 \ \mu m$ due to the longer simulation time. The laser pulse intensity in time and space has the form

$$I(t,y) = I_0 \sin^2\left(\pi t / 2\tau_{FWHM}\right) \exp\left(-(y/r_0)^2\right), \text{ where } r_0 = \frac{1}{2\sqrt{ln(2)}} D_{FWHM} \text{ is the focal spot radius at}$$

$1/e$ level. The parameters D_{FWHM} and τ_{FWHM} are the full width at half maximum (FWHM) laser spot size and pulse duration, respectively. The focal spot size for the three laser cases is the same, 5 μm. For sin^2 profile the total length of the pulse at the base is $2\tau_{FWHM}$. The laser energy is calculated by integrating the laser intensity profile in time and space, leading to the analytical formula $\varepsilon_{laser} = \pi r_0^2 I_0 \tau_{FWHM} \cong 1.13 D_{FWHM}^2 I_0 \tau_{FWHM}$. The laser pulse propagates in the "+x" direction and is linearly polarized in the "y" direction. Time $t = 0 \, fs$ denotes the time the laser pulse reaches the target. Particles are initialized with charge +1 for ions and −1 for electrons and kinetic energy 1 eV. The plasma is thus initially cold, having negligible internal energy prior to the interaction.

During the simulations the charge of oxygen and gold ions is dynamically incremented due to ionization. Tunneling ionization is modelled using the Ammosov-Delone-Krainov (ADK) ionization rate equation [34,35]. It is applied for each ion using the electric field strength at the location of the (ion) computational particle. Collisional ionization rates for ions are calculated using cell-averaged electron density, energy and velocity, and ionization cross section based on the Lotz formula [36]. Though the degree of accuracy vary depending on the ion charge state and atomic number [37], the

4

Lotz' formula has the advantage of being universal and computationally effective. Once computed, the tunneling and collisional ionization rates are tested for "ionization events" for every computational particle at every time step using a standard Monte Carlo scheme [37,38]. If a new ionization event occurs, the ion charge is incremented and a new electron computational particle is added at the location of the ion. Following this procedure, every computational particle acquires its own charge, which evolves in time.

The target thickness was chosen based on the following considerations. In general, the optimum foil thickness is laser pulse intensity and duration dependent. For example, it was previously established that for the Trident and Texas Petawatt lasers the optimum foil thickness is between 100 nm (simulations) and 200 nm (experiment) [39]. But the electron density in these cases was approximately 500 times the critical density, while for Au it is approximately 2500 times the critical density. To compensate for the higher electron density in Au, the foil thickness was scaled down. For the Bella laser, we estimate optimum thickness of 15 nm, based on the well-known criterion stating that the reduced thickness should equal the normalized laser field amplitude a_0 [15]. A compromise was reached by using the same foil thickness for the three laser systems. The value adopted was 20 nm.

One of the assumptions made in this work is that the targets do not pre-expand prior to the arrival of the main pulse. The laser contrast was taken to be high enough so that picosecond pre-pulses are below the damage threshold of the material. For gold, the damage threshold is approximately 0.5 J/cm^2, which for a 10-30 ps pre-pulse corresponds to intensity $(2\text{-}5)\times10^{10}$ W/cm^2. This requires a very high laser intensity contrast, better than 10^{10} on a picosecond time scale, compared to the main pulse. Such high contrast requirements are met by contemporary laser systems such as Hercules [40], Max Born Institute (MBI) High Field Ti:sapphire laser (MBI) [20], and the petawatt laser at the Institute for Basic Science in Gwangju, South Korea [41]. Using 20 nm foils is entirely feasible, considering that successful experiments using freestanding 14 nm gold foil have already been performed at the MBI facility. Nanosecond contrasts are not considered as many laser systems have managed to reduce them to levels well below the damage threshold.

Another simplification regarding the condition of the target is the contaminants on the foil surface. We consider only the contamination layer or the rear surface and omit the contamination layer at the front side. Additional simulations showed that the latter does not impede the acceleration of gold ions and the ions acceleration mechanisms retain its features. However, the contaminants on the rear surface must be included, as their impact on Au ion acceleration is significant [11].

Before presenting simulation results, it is worth recalling the main characteristics of RPA and

the other regime we call RIT. The initial stages of laser irradiation (the first few laser cycles) form highly overdense plasma in the focal spot, $n_e > \gamma n_{cr}$, where n_e and n_{cr} are the electron density and (non-relativistic) critical density, respectively, and γ is the relativistic parameter. The evolution of the plasma density later in time distinguishes RPA from RIT. The fundamental difference between RIT and the linear RPA is the plasma transparency to electromagnetic radiation. In the linear RPA regime, the plasma remains overdense and the laser pushes a double-layer structure of electrons and ions in a piston-like fashion. The electrons and ions form a co-moving sheath, which allows ions to be accelerated. In contrast, in RIT the longer pulse allows the highly overdense plasma to expand hydrodynamically and reduce its density. The main acceleration stage begins when the electron density drops sufficiently so that the plasma becomes relativistically transparent to the electromagnetic radiation ($n_e < \gamma n_{cr}$). If timing is right, (relativistic) transparency is reached near the peak of the laser intensity creating optimal conditions for ion acceleration. Because the target is transparent to the laser light, the electrons can regain energy lost for accelerating ions, a process leading to smooth continuous acceleration of ions residing in the focal spot. It is clear that one of the prerequisites for RIT is the plasma expansion. Since this process takes time, it is relevant for "long" pulses, on the order of 0.5-1 ps. For "short" pulses, < 50 fs, the plasma is likely to remain overdense for the duration of the laser pulse and if the foil is thin enough, the main ion acceleration mechanism is RPA. Since plasma transparency is the key, we will focus on it for the remainder of this section.

The presence of plasma transparency can be established by plotting the electron density in configuration space (*x,y*) and comparing it to the relativistically corrected critical density [21-23,27,28]. Similarly, the transmission of the laser pulse through the plasma can be assessed by looking at the electromagnetic pulse energy distribution with respect to the target. In Figure 2 we plot the normalized electron density n_e / n_{cr} and electromagnetic field energy density $\frac{\partial \varepsilon^{field}}{\partial V} = \frac{1}{2}\left(\varepsilon_0 \vec{E}^2(x,y) + \mu_0 \vec{H}^2(x,y)\right)$ for the three laser systems at the peak of the laser pulse. This specific time was chosen since the ionization stage ends and the acceleration stage begins roughly at that time.

For the shortest pulse (32 fs FWHM) the plasma in the laser focal spot remains overdense, i.e. $n_e > \gamma n_{cr}$ (Figure 2a), and the laser pulse is reflected from the foil. The transmission of the electromagnetic wave through the target is minimal (Figure 2b). Thus, the high plasma reflectivity creates conditions suitable for RPA. However, RPA may not be the only acceleration mechanism and contribution from TNSA is expected as well. Indeed, thin sheaths on both front and rear surface

are visible, suggesting that TNSA also plays a role. For linear laser polarization mixed TNSA-RPA regime is not uncommon [17], therefore, it is instructive to evaluate the role played by TNSA. Following the procedure outlined in Ref. [42], one can estimate the maximum (cut-off) energy that can be gained by ions in the rear side sheath, which is $E_{i,\max} = 2\overline{q}_i T_{hot} \ln^2(\tau + \sqrt{\tau^2 + 1})$, where $\tau \cong 0.43\omega_{pi}\tau_{acc}$ is the normalized acceleration time, $\omega_{pi} = \sqrt{4\pi n_{e,0} q_i e^2 / M_i}$ is the ion plasma frequency, and $T_{hot} \cong (\gamma - 1)m_e c^2$ and $n_{e,0} = N_{e,0}/(c\tau_{FWHM}S_{sheath})$ are the temperature and density of "hot" electrons launched at the front surface. For thin foils with no ballistic spreading of "hot" electrons, the sheath area $S_{sheath} = \pi D_{FWHM}^2 / 4$ and number $N_{e,0} = f\varepsilon_{laser} / T_{hot}$ yield for the "hot" electron density $n_{e,0} = fI_0/(cT_{hot})$, where f is the conversion efficiency of laser energy into "hot" electrons. Assuming f=30% conversion efficiency, one gets $T_{hot} \cong 20\,MeV$, $n_{e,0} \simeq 1\times10^{22}\,cm^{-3}$ and $\omega_{pi} = 1.3\times10^{14}\sqrt{q_i/M_i}\,s^{-1}$. Taking $\tau_{acc} = \tau_{FWHM}$, the normalized acceleration time for protons and Au^{60+} is 1.8 and 1.0, respectively, yielding maximum energies $E_{p,\max} \cong 72\,MeV$ and $E_{Au,\max} \cong 1.5\,GeV$ for protons and Au^{60+} ions. The estimate for the maximum proton energy is consistent with the PIC simulation results (~80 MeV). For Au^{56+} ions, however, it is well below the energies seen in simulations (Figure 3b), ruling out TNSA as the major acceleration mechanism of gold ions.

For the longest pulse case (600 fs FWHM) at the peak of the laser pulse the normalized plasma density $n_e/n_{cr} < 10$ becomes less than the laser field strength a_0=19, i.e. the plasma has expanded sufficiently to become relativistically transparent to the laser radiation. Thus transparency is reached at the beginning of the acceleration phase (Figure 2f). For the intermediate pulse length (180 fs FWHM), the plasma density is on the order of the relativistic critical density (Figure 2c). Because the plasma density does not fall below critical even though some plasma expansion has taken place, the laser pulse is mostly reflected (Figure 2d). The plasma and laser pulse conditions for the intermediate case are somewhat closer to that of the short pulse, but the analysis is inconclusive and the acceleration mechanism may be a mixture of RPA and RIT. We conclude that for the Bella laser the ion acceleration mechanism is RPA admixed with TNSA, for the Trident laser it is RIT and the Texas Petawatt laser is near the transition point.

3. Ion beam characteristics for the Bella, Texas Petawatt and Trident lasers

Numerical simulations for the three selected laser systems are presented in this section,

focusing on key ion beam parameters of practical interest such as flux, spectrum, charge distribution, and angular distribution. We consider only Au ions with kinetic energy >100 MeV (>0.5 MeV/nucleon) lying within 10 degrees half-angle from the target normal, which corresponds to solid angle $d\Omega = 0.095\,sr$. We shall refer to these ions as *forward accelerated*. The ion beam quality can be assessed by its angular distribution. Low-energy ions (protons and gold ions) have been eliminated from the analysis by collecting only ions with energy >0.5 MeV/nucleon.

Selected results for the Bella laser are shown in Figures 3 and 4. It has the highest intensity and the shortest pulse duration among the three laser systems modeled in this work. The momentum distribution of gold ions and spectrum in the forward direction at the end of the simulations (320 fs) are shown in Figure 3. Most of the ions are accelerated in the forward direction, but there is a substantial component of ions scattered backwards, toward the laser. The spectrum of gold ions, $\dfrac{d^2N}{dEd\Omega}$, is plotted in Figure 3b. The energy distribution is exponential with a cutoff energy of ~5 GeV (~25 MeV/nucleon). The calculated flux is $\dfrac{dN}{d\Omega} \cong 2\times10^{11}\,\dfrac{ions}{sr}$ and the conversion efficiency into the forward directed ion beam is 7-8 %. The ion charge vary between 33 and 68 with maximum number of ions having charge q=51 (Figure 4a). The pileup occurs when the next charge state has ionization potential too large to be overcome by optical field ionization. Beyond that, charges are formed primarily as a result of collisional ionization. The average charge-to-mass ratio is rather low, $\bar{q}/M \approx 0.25$, and the maximum charge-to-mass ratio for gold ions is $\left(q/M\right)_{max} \approx 0.34$. The angular distribution consists of two narrow peaks at 0 and 180 degrees (Figure 4b). The highly collimated beams emitted perpendicular to the foil surface can be advantageous for achieving large fluxes in either forward or backward directions. While the forward-directed beam can be explained within the standard theories of ion acceleration, we surmise that the backward-directed group of ions is due to Coulomb explosion of the Au layer [15]. The ions located initially in the compression layer will undergo RPA and will be snow-plowed forward because for these ions the electrostatic pressure balances the radiation pressure, while the ions left behind in the electron depletion layer will Coulomb explode in the backward direction.

Analogous results for the Texas Petawatt Laser are shown in Figures 5 and 6. They are very similar to the Bella laser with two exceptions: the angular distribution of gold ions is broader for the Texas Petawatt Laser and the number of backscattered ions is larger. The laser system with the longest pulse duration (600 fs FWHM) considered in this work, is the Trident laser, which has been

extensively used for ion acceleration in the BoA and RIT regimes. In all cases the long pulse (180 laser cycles) ensured long continuous acceleration of electrons and ions. Our simulations show that the same reasoning applies to heavy ions. Qualitatively, the momentum distribution and spectrum of gold ions are similar to that of the Bella and Texas Petawatt lasers, but the energies are higher (Figures 7 and 8). The angular distribution of gold ions on the Trident laser is, however, broader. Perhaps this is a result of Coulomb explosion of the ions in the forward moving bunch, which yields a transverse momentum. This effect is most pronounced for the Trident laser due to the longer acceleration time.

The ion beam quality can be assessed by the ion density distribution (Figure 9). The ion beam moving in the forward direction is split into two distinct parts going at an approximately 45 degree angle with respect to the laser beam axis. No such splitting was seen when the focal spot was twice larger. Splitting effects were previously observed in simulations with thin (10-20 nm) carbon foils. A very low focusing f-number of the laser beam (f/0.8), i.e. a very small focal spot, leads to beam breakup. Conversely, larger f-number (f/2) (larger focal spot) focusing preserved the ion beam integrity [43]. Ion beam splitting and ring-like structures of ion beams from Al foil at similar laser conditions was observed by Padda *et. al.* [27]. Figure 9 strongly indicates that for generation of high-quality heavy ion beams the focal spot must be large, on the order of 8-10 μm. The ion beam quality may be adversely affected by focal spot size reduction, a procedure often used to increase the laser intensity. Obviously, a tradeoff must be considered: large focal spot to keep high ion beam quality at reduced laser intensity, or smaller focal spot at higher intensity sacrificing (to some extend) the quality of the beam.

4. RPA-to-RIT transition point

In Sections 2 and 3 we discussed *specific* laser systems and the ion acceleration mechanism attributed to each one of them. The weakness of this approach is that too many input parameters were varied simultaneously (e.g. peak intensity and pulse duration), which does not allow a smooth transition from one ion acceleration mechanism to another. For this reason we fix the laser intensity to the highest value used in our simulations ($I_0 = 3 \times 10^{21}$ W/cm^2) and vary only the laser pulse duration in order to numerically determine the RPA-to-RIT transition point. In addition to the actual pulse length for Bella, $\tau_{FWHM} = 32\,fs$, we performed simulations with pulse lengths 120, 240 and 480 fs. For diagnostics we use the electromagnetic field energy density $\partial \varepsilon^{field}(x,y,t)/\partial V$ at the peak of the laser pulse ($t = \tau_{FWHM}$) to monitor the transmission of the laser pulse through the target. Figure 10 plots $\partial \varepsilon^{field}/\partial V$ for the four pulse durations. For $\tau_{FWHM} = 32\,fs$ the laser pulse is reflected (Fig.

10a), while for $\tau_{FWHM} = 120\,fs$ (Fig. 10b) there is a faint transmission of electromagnetic energy behind the target. It is limited to the laser axis only (y=64 μm), where the laser intensity is highest, and is smaller than the focal spot size. But since some amount of electromagnetic energy "leaks" through the target, it can be considered as the transition point from RPA to RIT. For the longer pulse durations, 240 and 480 fs, the laser pulse is clearly transmitted through the target, i.e. RIT has taken place. We conclude that for peak laser intensity I_0=3×10^{21} W/cm^2 the two ion acceleration regimes can be separated as follows:

$$\tau_{FWHM} < 120\,fs \Rightarrow RPA$$
$$\tau_{FWHM} > 120\,fs \Rightarrow RIT \tag{1}$$

It is likely that the transition point from RPA to RIT may depend upon the laser intensity. For peak laser intensity I_0=1×10^{21} W/cm^2 transmission of laser pulse energy through the target occurs for pulse duration ~200 fs; apparently for this (lower) intensity one needs longer pulse duration to reach the transition point. At even lower intensity, I_0=3×10^{20} W/cm^2, the transition point occurs for pulse duration $\tau_{FWHM} \cong 360\,fs$ (Figure 11). At this intensity, the shorter pulses, 120 and 240 fs, were unable to break through the target. In analogy to formula (1), we can write for peak laser intensity I_0=3×10^{20} W/cm^2:

$$\tau_{FWHM} < 360\,fs \Rightarrow RPA$$
$$\tau_{FWHM} > 360\,fs \Rightarrow RIT \tag{2}$$

A crude, but useful formula can be extracted from the three sets of simulations. The pulse duration demarcating RPA from RIT can be written in form

$$\tau_{FWHM}^{RPA \rightarrow RIT} \cong 210 I_{21}^{-1/2}\,fs \;, \tag{3}$$

where I_{21} is the peak laser intensity divided by 10^{21} W/cm^2. Formula (3) is only approximate and valid for the foil thickness considered in this work (20 nm).

5. Charge-to-mass ratio

In this section we revisit one of the critical parameters for ion acceleration: the charge-to-mass ratio. It is very unfavorable for ions having low q/M, e.g. for heavy ions, an issue that was brought up in the Introduction Section and in Section 3, where it was shown that for Au q/M is limited to about 0.3 for the laser intensities considered in this paper. The importance of the charge-to-mass ratio on the maximum ion energy (per nucleon) prompted us to look into this issue in more detail. Since the charge distribution of gold ions is relatively narrow and the number of ions in each charge state except q=51 is small, we decided to include information for ions from the contaminant layer on the back surface of the foil, i.e. protons and oxygen ions. Another reason is the ever-existing

competition between contaminants and ions from the bulk, which must be understood in order to choose proper conditions favoring the heavy ions [11]. In Figure 12 we plot the maximum energy per nucleon versus charge-to-mass ratio for protons, oxygen and gold ions. Due to the high laser intensity in the focal spot it stands to reason to take fully ionized oxygen having charge-to-mass ratio of 0.5. For gold ions we adopted the value 0.3, which corresponds to the highest charge-to-mass ratio. We observe a nearly linear dependence between the energy per nucleon and charge-to-mass ratio:

$$\left(\frac{E}{M}\right)_{max} \sim \left(\frac{q}{M}\right)_{max}. \tag{4}$$

Our findings are in contrast to previous studies, which showed a much stronger (quadratic) dependence [18,19]. We attribute this difference in scaling to the difference in ion acceleration mechanism. The quadratic scaling, $(E/M)_{max} \sim (q/M)^2$, is more typical for TNSA in which the ions are subjected to the sheath field on the rear side of the foil. This arrangement strongly favors the light ions. In our work the foil is ultrathin, only 20 nm, and comparable to the skin depth. The laser field can penetrate all the way to the back of the foil and accelerate ions from both the bulk and contaminant layer simultaneously. The charge-to-mass ratio is still unfavorable for heavy ions, but to a lesser extent. Another possibility for the different scaling is that we compare ions from a single simulation run, while in previous works comparison was made for ions subjected to different conditions (e.g. different laser and foil parameters).

6. Discussion and conclusions

The main purpose of the numerical simulations performed in this work is to elucidate the ion acceleration mechanisms and quantify the ion beam parameters for laser systems having pulse duration spanning from femtosecond to picosecond. We established that RPA is the mechanism that can be attributed to the shortest pulse, RIT to the longest, and in the intermediate case the mechanism remains somewhat undetermined. We surmise that it is a mixture of RIT and RPA. Qualitatively, the RIT mechanism works for both light and heavy ions, but there are quantitative differences. For RIT to work efficiently, the plasma expansion must be timed well so that transparency is reached near the peak of the laser pulse. For plasmas consisting of heavy ions the plasma density is higher and during the initial stage of the interaction the Coulomb attraction between highly charged ions and electrons may slow the plasma expansion and transparency may occur at a later time. This effect can be compensated for by using thinner targets. In general, the optimum foil thickness scales inversely with the atomic number of the material.

The gold ion energy spectra computed in this work are all exponential, reminiscent of TNSA. Manifestation of exponential spectra does not contradict the hypothesis of having RPA or RIT as the leading acceleration mechanisms; note that for gold the ion charge spread is large (a factor of two), which is likely to broaden energy distribution. A distribution with narrow energy spread is more likely to occur when a single ionization state is present, as was the case with aluminum [25]. Moreover, RPA, RIT and other acceleration mechanisms are always mixed with TNSA to some extent [17]. The simulation results for the ion beam parameters from the three laser systems considered in this work, Bella, Texas Petawatt and Trident lasers, are summarized in Table 2. For gold ions the fluxes in the forward direction are comparable, on the order of 10^{11} ions/sr, and not directly related to the laser energy on target. The maximum energy vary between 25 and 50 MeV/nucleon with the highest energy recorded for the laser system with the longest pulse duration (Trident). The same holds for protons (originating from the contaminant layer), except the proton flux is one order of magnitude larger than the flux of gold ions (from the bulk of the foil).

Transition from RPA to RIT occurs for pulse duration on the order of a few hundred femtoseconds (FWHM), depending upon peak laser intensity. The numerical simulations indicate that the transition point scales as $\tau_{RPA \to RIT} \sim \sqrt{1/I_0}$.

In conclusion, using a 2D PIC code we have demonstrated theoretically the possibility of laser-driven heavy ion beams with energies of up to 45 MeV/nucleon from ultrathin (20 nm) planar foils. Numerical simulations performed for three lasers systems show that: (i) the ion acceleration mechanism depends on the laser pulse duration. They are akin to those for light ions and protons, however, nuances of the acceleration process exist. Two-stage ion acceleration (ionization phase followed by acceleration phase) distinguishes heavy from light ions; (ii) all laser systems are suitable for heavy ion acceleration, which is due to the large amount of energy (>20 J) delivered on target; (iii) the charge distribution of gold ions is practically independent of the laser system. The charge-to-mass ratio spread from 0.16 to 0.32 with the majority of ions having charge q=51 (q/M≈0.25); and (iv) unlike previous studies, we observe linear increase of the maximum energy per nucleon with charge-to-mass ratio.

Figure captions:

Figure 1. A sketch of the computational domain and target location. The laser and foil parameters for Bella, Texas Petawatt and Trident lasers are listed in Table 1.

Figure 2. Normalized electron density and electromagnetic field energy per unit volume for Bella (a,b), Texas Petawatt (c,d) and Trident lasers (e,f). The dashed horizontal lines denote the laser focal spot and the dashed vertical line at x_0=48 μm denotes the position of the foil.

Figure 3. Momentum distribution of gold ions (a) and energy spectrum of forward accelerated gold ions (b) at the end of the simulations for the Bella laser. Only ions with energy >100 MeV within solid angle $d\Omega = 0.095\,sr$ are included.

Figure 4. Charge distribution of forward accelerated gold ions (a) and angular distribution of gold ions (b) at the end of the simulations for the Bella laser.

Figure 5. Momentum distribution of gold ions (a) and energy spectrum of forward accelerated gold ions (b) at the end of the simulations for the Texas Petawatt Laser. Only ions with energy >100 MeV within solid angle $d\Omega = 0.095\,sr$ are included.

Figure 6. Charge distribution of forward accelerated gold ions (a) and angular distribution of gold ions (b) at the end of the simulations for the Texas Petawatt Laser.

Figure 7. Momentum distribution of gold ions (a) and energy spectrum of forward accelerated gold ions (b) at the end of the simulations for the Trident laser. Only ions with energy >100 MeV within solid angle $d\Omega = 0.095\,sr$ are included.

Figure 8. Charge distribution of forward accelerated gold ions (a) and angular distribution of gold ions (b) at the end of the simulations for the Trident laser.

Figure 9. Density of gold ions (in units 10^{19} cm^{-3}) at the end of the simulations for the Trident laser. Only ions with energy >100 MeV are included. The dashed vertical line denotes the foil position. The dotted horizontal lines denote the laser focal spot.

Figure 10. Electromagnetic field energy per unit volume at the peak of the laser pulse for peak laser intensity I_0=3×10^{21} W/cm^2 and pulse durations 32 (a), 120 (b), 240 (c) and 480 fs (d). The target is located at spatial position x_0=48 μm.

Figure 11. Electromagnetic field energy per unit volume at the peak of the laser pulse for peak laser intensity I_0=3×10^{20} W/cm^2 and pulse durations 120 (a), 240 (b), 360 (c) and 480 fs (d). The target is located at spatial position x_0=48 μm.

Figure 12. Maximum energy per nucleon versus charge-to-mass ratio for Bella, Texas Petawatt and Trident laser systems.

13

Table 1. Laser, target and computational parameters used in the simulations.

parameter	variable & units	Bella	TPW	Trident
laser intensity	$I_0\ (W/cm^2)$	3×10^{21}	1×10^{21}	5×10^{20}
pulse duration	$\tau_{FWHM}\ (fs)$	32	180	600
focal spot size	$D_{FWHM}\ (\mu m)$	5	5	5
wavelength	$\lambda\ (\mu m)$	0.8	1	1
energy	$\varepsilon_{laser}\ (J)$	27	50	85
a_0, γ		37	27	19
foil thickness	$L\ (nm)$	20	20	20
foil width	$W\ (\mu m)$	126	126	254
foil location	$x_0\ (\mu m)$	48	48	48
computational domain	$L_x \times L_y\ (\mu m^2)$	100x128	100x128	200x256
cell size	$\Delta x \times \Delta y\ (nm^2)$	20x20	20x20	20x20
time step	$\Delta t\ (\lambda/c)$	0.005	0.005	0.005
simulation time	$t_{sims}\ (fs)$	320	540	1200

Table 2. Calculated flux $dN/d\Omega$, maximum energy per nucleon $(E/M)_{max}$ and conversion efficiency η for protons and gold ions moving in the forward direction. The full laser and foil parameters are listed in Table 1.

parameter	variable & units	Bella	TPW	Trident
pulse duration	$\tau_{FWHM}\ (fs)$	32	180	600
energy	$\varepsilon_{laser}\ (J)$	27	50	85
Au ions	$dN/d\Omega$ (ions/sr)	1.7×10^{11}	3.0×10^{11}	2.6×10^{11}
	$(E/M)_{max}$ (MeV/nucleon)	25	29	50
	η (%)	7.4	8.4	6.6
protons	$dN/d\Omega$ (ions/sr)	2.2×10^{12}	1.3×10^{12}	1.2×10^{12}
	$(E/M)_{max}$ (MeV/nucleon)	85	115	120
	η (%)	2.0	1.4	0.4

1
2
3
4
5
6
7
8
9
10
11
12
13
14
15
16
17
18
19
20

Figure 1

21
22
23
24
25
26
27
28
29
30
31
32
33
34
35
36
37
38
39
40
41
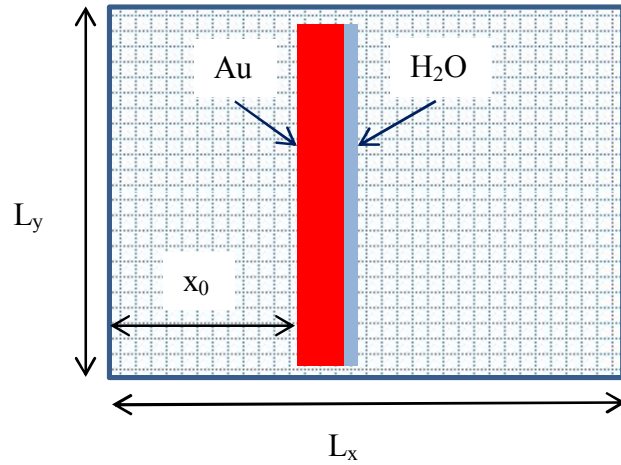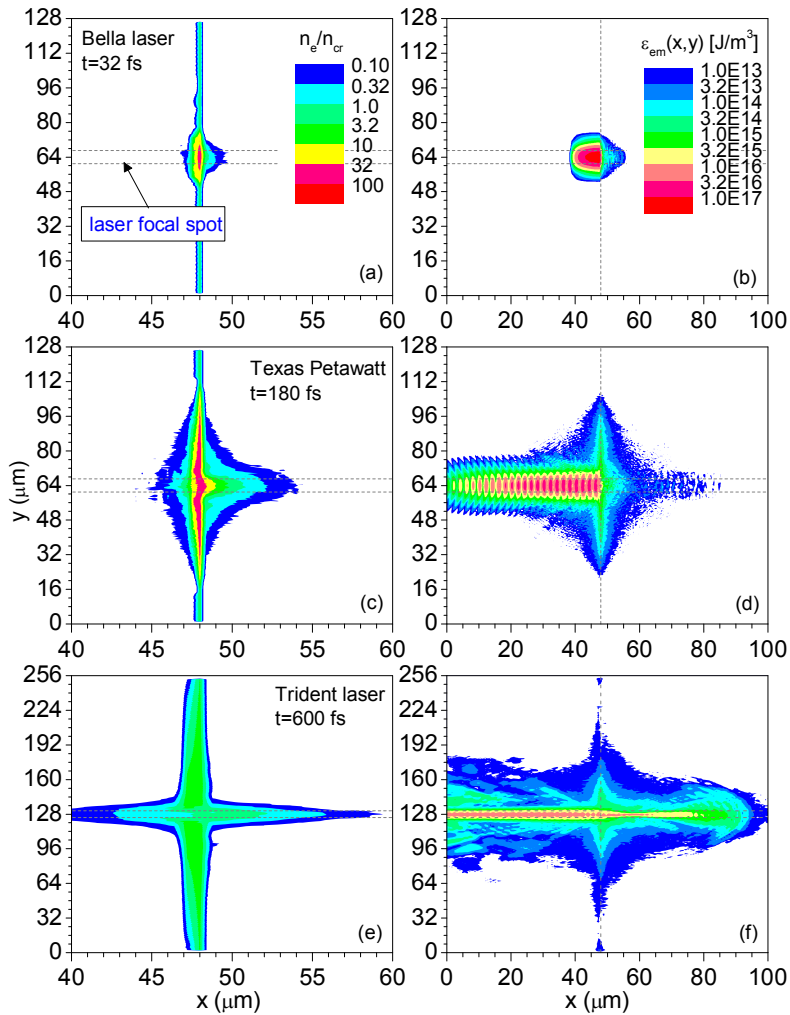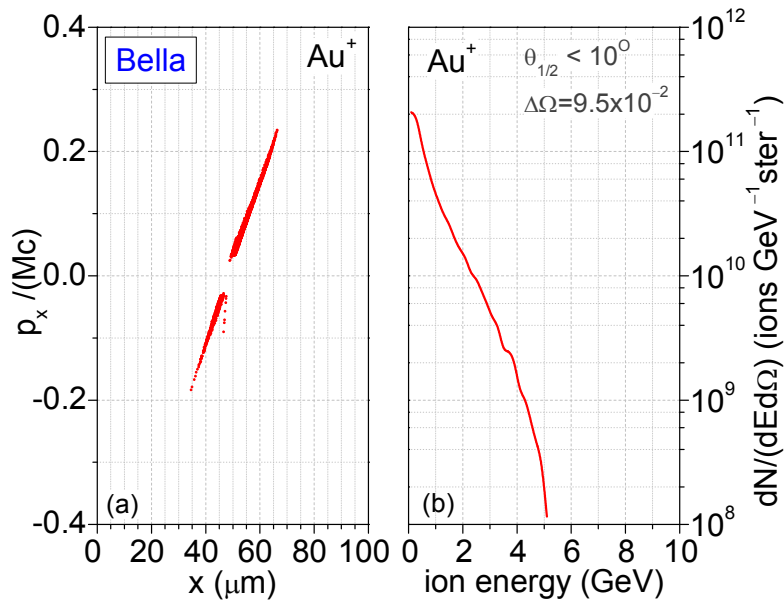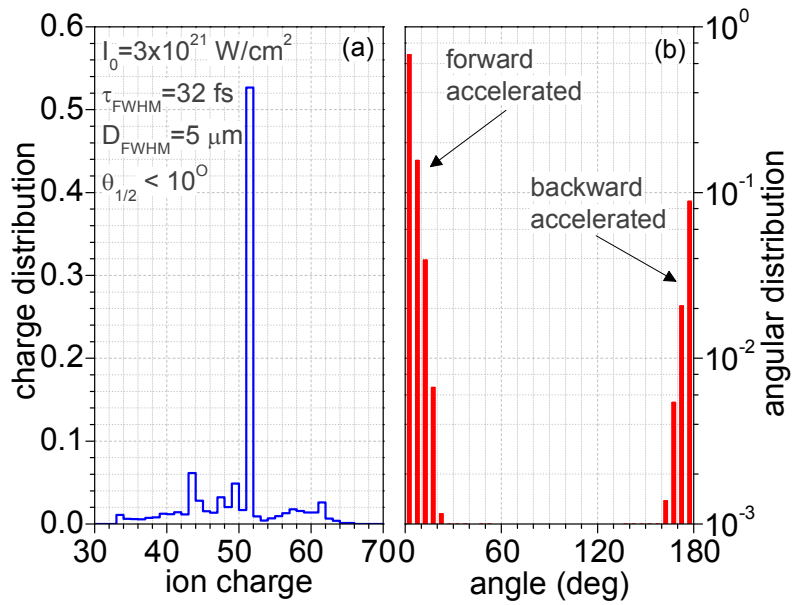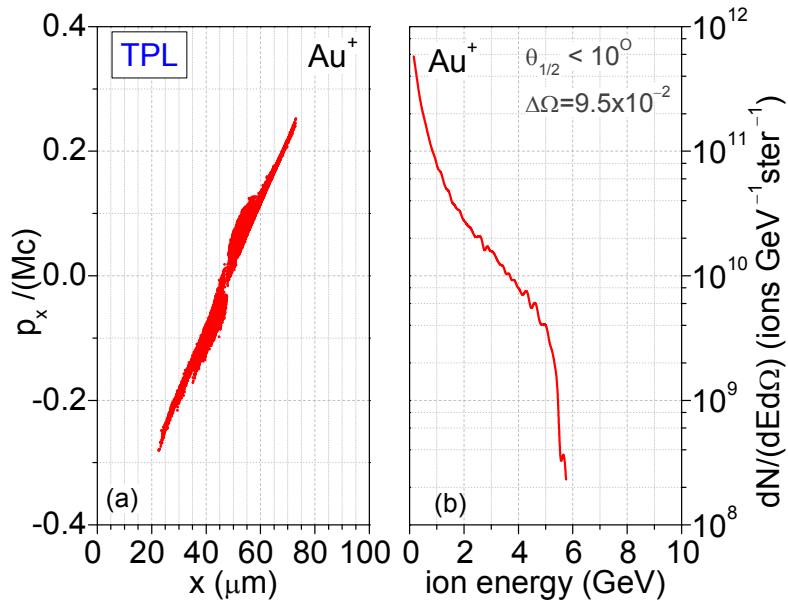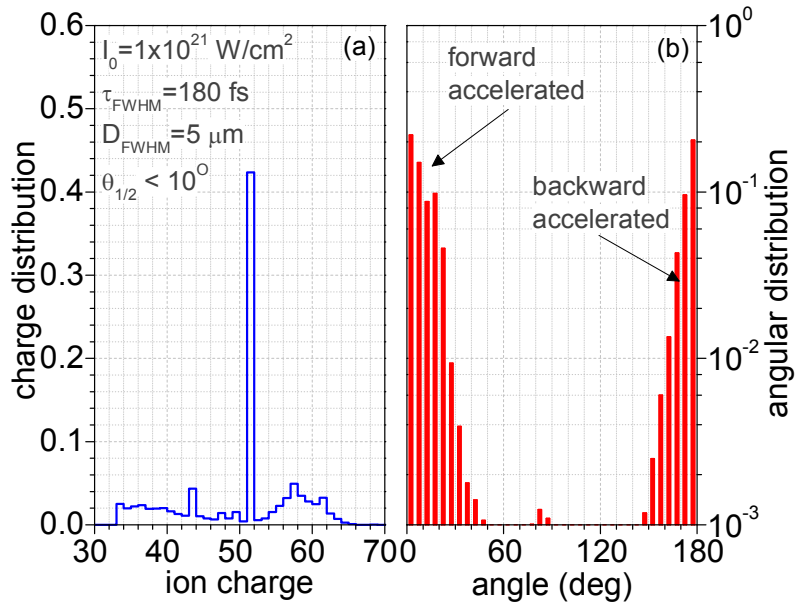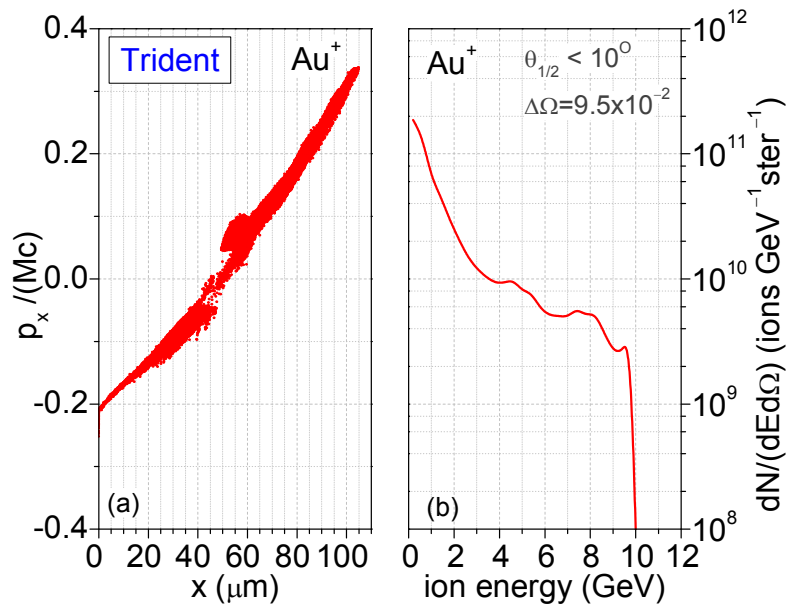42
43
44
45
46
47
48
49
50
51
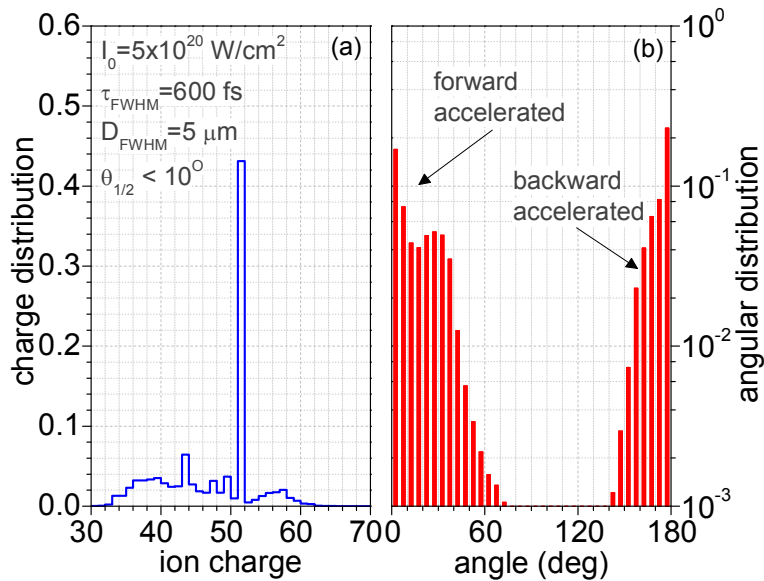52
53
54
55

Figure 2

56
57
58
59
60

Figure 3

Figure 4

16

Figure 5

Figure 6

Figure 7

Figure 8

1
2
3
4
5
6
7
8
9
10
11
12
13
14
15
16
17
18
19
20
21
22
23
24
25
26
27
28
29
30
31
32
33
34
35
36
37
38
39
40
41
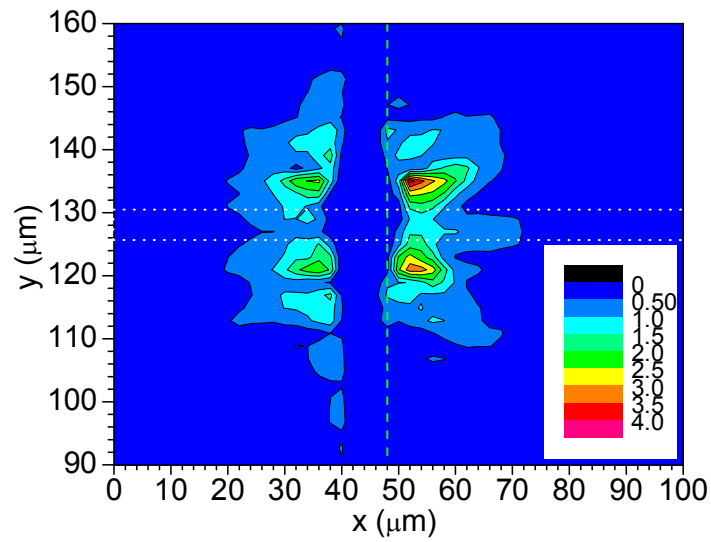42
43
44
45
46
47
48
49
50
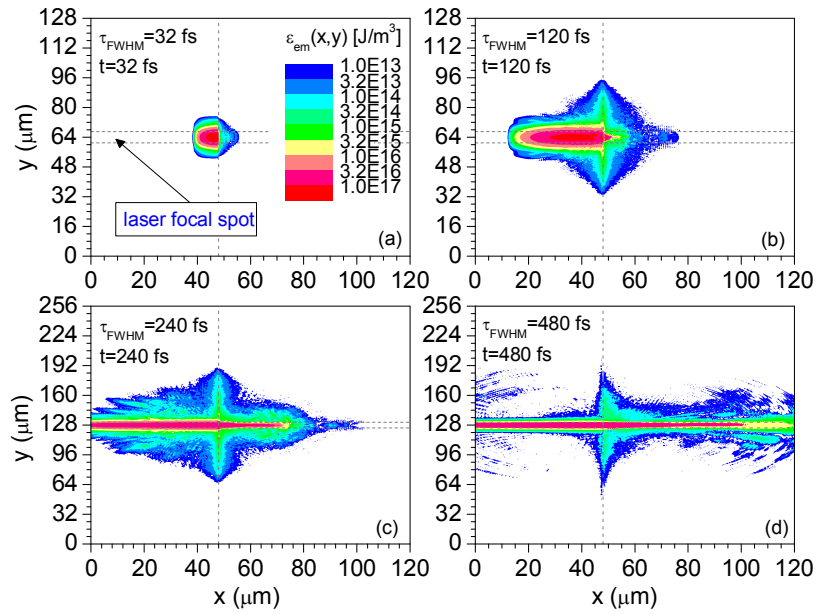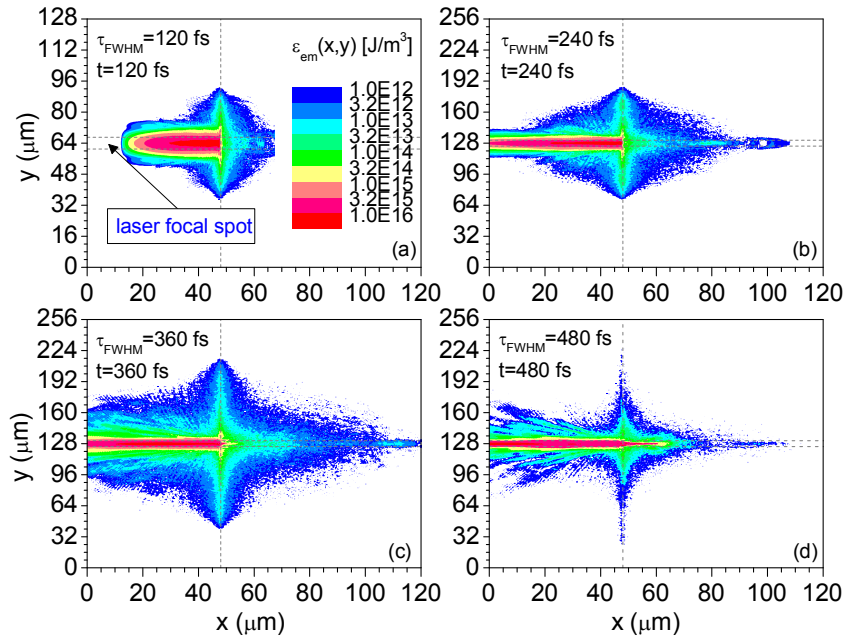51
52
53
54
55
56
57
58
59
60

Figure 9
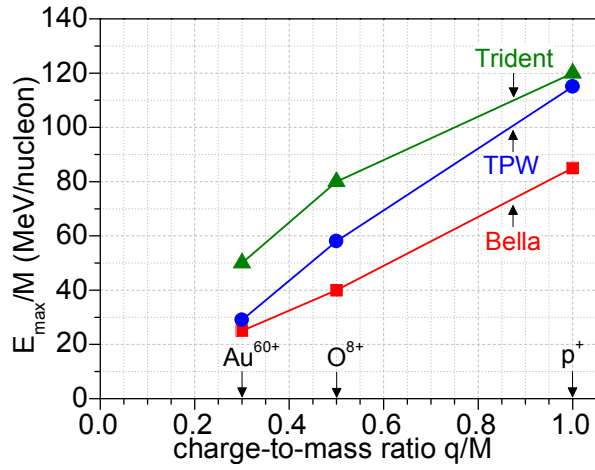
Figure 10

Figure 11

Figure 12

References:

1 Flerov G N and Barashenkov V S 1975 Sov. Phys. Usp. **17** 783

2 Ledingham K W D, McKenna P and Singhal R P 2003 Science **300** 1107

3 Baba M 2006 Nuclear Eng. Tech. **38** 319

4 McKenna P, Ledingham K W D, McCanny T, Singhal R P, Spencer I, Santala M I K, Beg F N, Krushelnick K, Tatarakis M, Wei M S, Clark E L, Clarke R J, Lancaster K L, Norreys P A, Spohr K, Chapman R and Zepf M 2003 Phys. Rev. Lett. **91** 075006

5 McKenna P, Ledingham K W D, Yang J M, Robson L, McCanny T, Shimizu S, Clarke R J, Neely D, Spohr K, Chapman R, Singhal R P, Krushelnick K, Wei M S and Norreys P A 2004 Phys. Rev. E **70**, 036405

6 Habs D Thirolf P G, Gross M, Allinger K, Bin J, Henig A, Kiefer D, Ma W and Schreiber J 2011 Appl. Phys. B **103** 471

7 Patel P K, Mackinnon A J, Key M H, Cowan T E, Foord M E, Allen M, Price D F, Ruhl H, Springer P T and Stephens R 2003 Phys. Rev. Lett. **91** 125004

8 Ledingham K W D 2006 Hyperfine Interact **171** 69

9 Kramer D 2015 Phys. Today **68** 24

10 Nishiuchi M, Sakaki H, Esirkepov T Zh, Nishio K, Pikuz T A, Faenov A Ya, Skobelev I Yu, Orlandi R, Sako H, Pirozhkov A S, Matsukawa K, Sagisaka A, Ogura K, Kanasaki M, Kiriyama H, Fukuda Y, Koura H, Kando M, Yamauchi T, Watanabe Y, Bulanov S V, Kondo K, Imai K and Nagamiya S 2015 Phys. Plasmas **22**, 033107

11 Petrov G M, McGuffey C, Thomas A G R, Krushelnick K and Beg F N 2016 Phys. Plasmas **23**, 063108

12 Wilks S C, Langdon A B, Cowan T E, Roth M, Singh M, Hatchett S, Key M H, Pennington D, MacKinnon A and Snavely R A 2001 Phys. Plasmas **8** 542

13 Wilks S C, Kruer W L, Tabak M and Langton A B 1992 Phys. Rev. Lett. **69** 1383

14 Qiao B, Zepf M, Borghesi M and Geissler M 2009 Phys. Rev. Lett. **102** 145002

15 Macchi A, Veghini S and Pegoraro F 2009 Phys. Rev. Lett. **103** 085003

16 Henig A, Steinke S, Schnürer M, Sokollik T, Hörlein R, Kiefer D, Jung D, Schreiber J, Hegelich B M, Yan X Q, Meyer-ter-Vehn J, Tajima T, Nickles P V, Sandner W and Habs D 2009 Phys. Rev. Lett. **103** 245003

17 Qiao B, Kar S, Geissler M, Gibbon P, Zepf M and Borghesi M 2012 Phys. Rev. Lett. **108** 115002

18 McKenna P, Lindau F, Lundh O, Carroll D C, Clarke R J, Ledingham K W D, McCanny T, Neely D, Robinson A P L, Robson L, Simpson P T, Wahlstrom C-G and Zepf M 2007 Plasma Phys. Contr. Fusion **49** B223

19 Schreiber J, Bell F, Gruner F, Schramm U, Geissler M, Schnurer M, Ter-Avetisyan S, Hegelich B M, Cobble J, Brambrink E, Fuchs J, Audebert P and Habs D 2006 Phys. Rev. Lett. **97** 045005

20 Braenzel J, Andreev A A, Platonov K, Klingsporn M, Ehrentraut L, Sandner W and Schnürer M 2000 Phys. Rev. Lett. **114** 124801

21 Yin L, Albright B J, Hegelich B M and Fernández J C 2006 Laser Part. Beams **24** 291

22 Yin L, Albright B J, Hegelich B M, Bowers K J, Flippo K A, Kwan T J T and Fernandez J C 2007 Phys. Plasmas **14** 056706

23 Yin L, Albright B J, Jung D, Shah R C, Palaniyappan S, Bowers K J, Henig A, Fernandez J C and Hegelich B M 2011 Phys. Plasmas **18** 063103

24 Jung D, Yin L, Albright B J, Gautier D C, Letzring S, Dromey B, Yeung M, Horlein R, Shah R, Palaniyappan S, Allinger K, Schreiber J, Bowers K J, Wu H-C, Fernandez J C, Habs D and Hegelich B M 2013 New J. Phys. **15** 023007

25 Palaniyappan S, Huang C, Gautier D C, Hamilton C E, Santiago M A, Kreuzer C, Sefkow A B, Shah R C and Fernandez J C 2015 Nature Comm. **6**, 10170

26 Henig A, Kiefer D, Markey K, Gautier D C, Flippo K A, Letzring S, Johnson R P, Shimada T, Yin L, Albright B J, Bowers K J, Fernandez J C, Rykovanov S G, Wu H-C, Zepf M, Jung D, Liechtenstein V Kh, Schreiber J, Habs D, and Hegelich B M 2009 Phys. Rev. Lett. **103** 045002

27 Padda H, King M, Gray R J, Powell H W, Gonzales-Izquierdo B, Stockhausen L C, Wilson R, Carroll D C, Dance R J, MacLellan D A, Yuan X H, Butler N M H, Capdessus R, Borghesi M, Neely D and McKenna P 2016 Phys. Plasmas **23**, 063116

28 Gonzales-Izquierdo B, King M, Gray R J, Wilson R, Dance R J, Powell H, MacLellan D A, McCreadie J, Butler N M H, Hawkes S, Green R J, Murphy C D, Stockhausen L C, Carroll D C, Booth N, Scott G G, Borghesi M, Neely D and McKenna P 2016 Nature Comm **7**, 12891

29 Hegelich B M, Albright B J, Audebert P, Blazevic A, Brambrink E, Cobble J, Cowan T, Fuchs J, Gauthier J C, Gautier C, Geissel M, Habs D, Johnson R, Karsch S, Kemp A, Letzring S, Roth M, Schramm U, Schreiber J, Witte K J and Fernández J C 2005 Phys. Plasmas **12** 056314

30 Hegelich B M, Albright B J, Cobble J, Flippo K, Letzring S, Paffett M, Ruhl H, Schreiber J, Schulze R K and Fernandez J C 2006 Nature **439** 441

31 Clark E L, Krushelnick K, Zepf M, Beg F N, Tatarakis M, Machacek A, Santala M I K, Watts I, Norreys P A and Dangor A E 2000 Phys. Rev. Lett. **85** 1654

32 Petrov G M and Davis J 2011 Phys. Plasmas **18** 073102

33 Petrov G M and Davis J 2014 Commun. Comput. Phys. **16** 599

34 Ammosov M, Delone N B and Krainov V P 1986 Sov. Phys. JETP **64** 1191

35 Penetrante B M and Bardsley J N 1991 Phys. Rev. A **43** 3100

36 Lotz W 1970 Z. Phys. **232** 101

37 Petrov G M, Davis J and Petrova Tz 2009 Plasma Phys. Control. Fusion **51** 095005

38 Kemp A J, Pfund R E W and Meyer-ter-Vehn J 2004 Phys. Plasmas **11** 5648

39 Hegelich B M, Pomerantz I, Yin L, Wu H C, Jung D, Albright B J, Gautier D C, Letzring S, Palaniyappan S, Shah R, Allinger K, Horlein R, Schreiber J, Habs D, Blakeney J, Dyer G, Fuller L, Gaul E, Mccary E, Meadows A R, Wang C, Ditmire T and Fernandez J C 2015 New J. Phys. **15** 085015

40 Dollar F, Zulick C, Matsuoka T, McGuffey C, Bulanov S S, Chvykov V, Davis J , Kalinchenko G, Petrov G M, Willingale L, Yanovsky V, Maksimchuk A, Thomas A G R and Krushelnick K 2013 Phys. Plasmas **20** 056703

41 Kim I J, Pae K H, Choi I W, Lee C-L , Kim H T, Singhal H, Sung J H, Lee S K, Lee H W, Nickles P V, Jeong T M, Kim C M and Nam C H 2016 Phys. Plasmas **23** 070701

42 Fuchs J, Antici P, d'Humières E, Lefebvre E, Borghesi M, Brambrink E, Cecchetti C A, Kaluza M, Malka V, Manclossi M, Meyroneinc S, Mora P, Schreiber J, Toncian T, Pépin H and Audebert P 2006 Nature Phys. **2** 48

43 Dover N P and Najmudin Z 2012 High Energy Density Physics **8** 170